MIT Open Access Articles

Observation of unidirectional backscattering-immune topological electromagnetic states

The MIT Faculty has made this article openly available. ***Please share*** how this access benefits you. Your story matters.

Citation	Wang, Zheng, Yidong Chong, J. D. Joannopoulos, and Marin Soljacic. "Observation of Unidirectional Backscattering-Immune Topological Electromagnetic States." Nature 461, no. 7265 (October 8, 2009): 772–775.
As Published	http://dx.doi.org/10.1038/nature08293
Publisher	Nature Publishing Group
Version	Author's final manuscript
Citable link	http://hdl.handle.net/1721.1/88469
Terms of Use	Creative Commons Attribution-Noncommercial-Share Alike
Detailed Terms	http://creativecommons.org/licenses/by-nc-sa/4.0/

Massachusetts Institute of Technology

DSpace@MIT

Observation of Unidirectional Backscattering-immune Topological Electromagnetic States

Zheng Wang[1*], Yidong Chong[1†*], J.D. Joannopoulos[1], Marin Soljačić[1]

One of the most striking phenomena in condensed-matter physics is the Quantum Hall Effect (QHE) arising in two-dimensional electron gases[1-4] subjected to a large DC magnetic field. The resulting "Chiral edge states" (CESs) are a unique class of states with unparalleled properties that have only been observed in *electronic* systems. Here we report the first experimental observation of *electromagnetic* CESs (existence first predicted by Haldane and Raghu[5,6]), exploiting a magneto-optic photonic crystal (PhC)[7] fabricated in the microwave regime. Like their electronic counterparts, these photonic CESs can travel in only one direction, and we measure forward and backward transmissions differing by nearly 50 dB. And, just as the electronic CESs are dissipationless even in the presence of impurities[8], we observe that even large metallic scatterers placed in the path of the photonic CESs do not induce reflections. Essentially, the electromagnetic waves losslessly "route around" the obstacles because the absence of backwards-propagating solutions prohibits any possibility of reflection. In both the electronic systems[9-13] and photonic systems[5-7], this unique form of unidirectional transport is a consequence of nontrivial topological properties of the bulk band structure. In this work we implement a photonic CES using a square lattice of magnetized ferrite rods that localize a unidirectional

[1] *Department of Physics, Massachusetts Institute of Technology, Cambridge, Massachusetts 02139.*

[†] Present address: Yale University, New Haven, Connecticut, 06520

[*] *These authors contributed equally to this work.*

waveguide mode at the edge of the structure adjacent to a metallic wall. We believe the realization of CESs in photonic systems opens a wide range of exciting opportunities for two reasons. First, photonic systems are easily modified into any imaginable geometry using a variety of materials, sources, and detectors, enabling observation of this exciting topological phenomenon in a much more controlled and customizable fashion than typically possible with electronic systems. Second, the unique nature of these unidirectional modes may enable new classes of electromagnetic devices and experiments that would be impossible using conventional reciprocal photonic states alone.

The existence of photonic CESs is predicted by an analogy between a PhC[14-16] with broken time-reversal symmetry and a QHE system[5-7]. In this analogy, the electromagnetic fields play the role of the electronic current, the variations of permittivity and permeability within the PhC play the roles of the periodic potential, and the gradients of the gyrotropic components of the permeability tensor play the role of the external DC magnetic field which breaks the time-reversal symmetry[5-7]. The defining feature of a photonic CES is that its group velocity points in only one direction, which is determined by the sign of the time-reversal symmetry breaking field and the resulting unusual topological properties of the bulk band structure. To detect the possible presence of non-trivial topological band properties in a PhC system it is *sufficient*[5-7] to compute its Chern numbers. (Although the original proposal[5,6] focused on "Dirac points", it is not *necessary* to be restricted to such band structures, and thus the use of a variety of PhC systems is possible[7].) The Chern number of a band *n* of a 2D periodic PhC is an *integer* defined by[6]:

$$C_n = \frac{1}{2\pi i}\int_{BZ} d^2k \left(\frac{\partial \mathrm{A}_y^{nn}}{\partial k_x} - \frac{\partial \mathrm{A}_x^{nn}}{\partial k_y} \right),$$

where the k-space integral is performed over the first Brillouin zone and the Berry connection[6] is given by:

$$\vec{\mathrm{A}}^{nn'}(\mathbf{k}) \equiv i\left\langle E_{n\mathbf{k}} \middle| \nabla_{\mathbf{k}} \middle| E_{n'\mathbf{k}} \right\rangle = i\int d^2 r \varepsilon(\mathbf{r}) E^*_{n\mathbf{k}}(\mathbf{r}) \cdot \nabla_{\mathbf{k}} E_{n'\mathbf{k}}(\mathbf{r}),$$

where $\mathbf{E}_{n\mathbf{k}}$ is the periodic part of the electric field Bloch function[16]. Since the Chern number characterizes the winding number of the phase of the Bloch functions around the boundary of the first Brillouin zone[11], it is a "global" or "topological" property of the entire band, and is very robust against structural perturbations[10]. Significantly, it can be non-zero if and only if the system lacks time-reversal symmetry[9]. One of the most exciting properties of QHE systems is that the Chern numbers have a direct physical consequence: a finite crystal that supports bulk bands with non-zero Chern numbers also supports unidirectional CESs at its boundary at energies within bulk band gaps opened by the applied DC magnetic field. Moreover, the number of CESs turns out to be equal *to the sum of the Chern numbers of all the bulk bands with lower energy*.[13] Although this result has been formally proven only in a tight-binding QHE system, it is believed to be independent of the details of the underlying model, such as the structure of the lattice and the edge. Its validity in PhC systems was originally predicted by Haldane and Raghu[5,6], and corroborated through a formal mapping[7] to a "zero-field QHE" system[12] and *ab initio* numerical simulations of Maxwell's equations[7]. It is important to emphasize that although CESs have so far been experimentally observed only in electronic (i.e. fermionic) systems, the phenomenon should actually be independent of the underlying particle statistics because the Chern number is defined in terms of *single*-particle Bloch functions. An experimental verification would therefore provide a strong support for generalizing topological band theories and their applications to classical and bosonic systems.

The ability to work with PhC band structures without "Dirac points" has allowed for the identification of an experimentally viable PhC system[7] for the observation of CESs. Our experimental system (Fig. 1) involves a gyromagnetic 2D-periodic PhC consisting of a square lattice of ferrite rods in air (details of the structure and materials used can be found in the section on Methods), bounded on one side by a non-magnetic metallic cladding. The interface between

the PhC and the cladding acts as a confining-edge or waveguide for CESs. (Without this cladding the CESs at the air edges of the PhC would simply radiate away.) Apart from absorption losses and nonlinear effects, we would expect power transmission of a CES along this waveguide to be independent of the waveguide geometry and also immune to back-scattering from disorder, obstacles, and defects.

Before we discuss the results of our measurements, we will first describe how we arrived at this particular choice of experimental system. We chose rods in air for the basic PhC geometry because of ease of fabrication. We then performed a series of numerical simulations for a variety of rod sizes and lattice constants on a model 2D PhC system to optimize the band structure and compute corresponding band Chern numbers using material parameters appropriate to a low-loss ferrite (see Methods). Our numerical simulations predict that when the ferrite rods in this PhC are magnetized to manifest gyrotropic permeability (which breaks time-reversal symmetry), a gap opens up between the second and third TM bands. Moreover the second, third, and fourth bands of this PhC acquire Chern numbers of 1, -2, and 1 respectively. This result follows from the C_{4v} symmetry of a non-magnetized crystal[17]. The results of our simulations for the PhC with metallic cladding are presented in Fig. 2. (Similar numerical results were obtained in ref. 7, albeit using a different material system and geometry.) Here we show the calculated field patterns of a photonic CES residing in the second TM band gap (between the second and the third bands). Since the sum of the Chern numbers over the first and second bands is *one*, exactly *one* CES is predicted to exist at the interface between the PhC and metal cladding. The simulations clearly predict that this photonic CES is unidirectional. Since side-scattering is prohibited by the bulk photonic band gaps in the PhC and in the metallic cladding, the existence of the CES forces the feed dipole antennas (which would radiate omnidirectionally in a homogeneous medium) to radiate only towards the right (Fig. 2a, c). Moreover, the lack of any backward propagating mode eliminates the possibility of backscattering, so that the fields can continuously navigate around an obstacle, as shown in Fig. 2b. Hence the scattering from the obstacle results only in a

change of the phase (compare Fig. 2a and Fig. 2b) of the transmitted radiation with no reduction in amplitude.

In order for CESs to be readily measurable in the laboratory (where one is forced to employ a PhC of finite and manageable size) they must be spatially well localized, and this requires a large containing photonic band gap. The sizes of the band gaps that contain CESs (and the frequencies at which they occur) are determined by the gyromagnetic constants of the ferrites constituting the PhC. Under a DC magnetic field, microwave ferrites exhibit a ferromagnetic resonance at a frequency determined by the strength of the external DC magnetic field[18]. Near this frequency, the Voigt parameter, $V = |\mu_{xy}| / |\mu_{xx}|$, a direct measure of the strength of the gyromagnetic effect, is of order unity. Such ferromagnetic resonances are among the strongest low-loss gyrotropic effects at room temperature and sub-Tesla magnetic fields. Using ferrite rods composed of vanadium-doped calcium–iron-garnet (VCIG) under a biasing magnetic field of 0.20 T (see Methods and supplementary information), we achieved a relative bandwidth of 6% for the second TM band gap (around 4.5 GHz in Fig. 3b). As discussed earlier, this is the gap predicted to support a CES at the interface of the PhC with a metallic wall. Let us emphasize again that band gaps with trivial topological properties (i.e., zero sum for the Chern numbers of the bulk bands with lower frequencies), such as the first TM band gap (around 3 GHz in Fig. 3b), do not support CESs. All of the insight gained from the model 2D PhC system was then incorporated into the final design shown in Fig. 1. To emulate the states of the 2D PhC the final design involved fabrication of a 3D PhC slab structure equivalent to the model 2D PhC system, made from gyromagnetic rods with parallel metallic plates on the top and bottom, spaced to only support TEM modes (identical to the TM modes in the 2D PhC, see Methods). A copper wall was then added at the edge of the PhC slab to provide the required cladding.

In our experiments the band gaps and the CES waveguide were characterized by two-port vector network analysis using a pair of dipole antennas labelled A and B in Fig. 1a (see

Methods). First, to characterize the band gap, we inserted A and B into the interior of the PhC far from the edges and 8 lattice constants apart. We observed the second band gap with a 50 dB extinction for both forward ($|S_{BA}|^2$) and backward ($|S_{AB}|^2$) transmission (Fig. 3a). Note that the frequency ranges of both first and second band gaps agree well with our predicted band structure calculations (no adjustable parameters) shown in Fig. 3b. Next, to characterize the CESs, we measured the transmission spectra with the apparatus as illustrated in Fig. 1a (see Methods). At frequencies within the second band gap, we observed a strong forward transmission, approximately 50 dB greater than the backward transmission at mid-gap frequencies (Fig. 3c). Over much of this frequency range, the backward transmission was below the noise floor of the network analyzer, which suggests an even greater actual contrast. This difference of more than 5 orders of magnitude in power transmission, over a distance of only 8 lattice constants, confirms that backward-propagating modes are highly evanescent, as predicted.

We tested the robustness of the unidirectional propagation by studying the effect of a large obstacle on transmission. We gradually inserted a conducting barrier across the waveguide, blocking the direct path between A and B. The measured transmission behaviour at different stages of the insertion, shown in Fig. 4, remains basically the same as that of Fig. 3c: the transmission between 4.35 and 4.62 GHz remains strongly non-reciprocal, with a 40 to 50 dB difference between the forward and backward transmission. This finding agrees with the theoretical prediction that power transmission via CESs is fundamentally insensitive to scattering from arbitrarily large defects (Fig. 2b). This behaviour is a distinguishing feature of the present waveguide. In a conventional waveguide, insertion of such a large obstacle would cause huge backscattering and dramatically reduced transmission to the output. For example, in a photonic crystal implemented with regular dielectric rods and identical dimensions (see supplementary information), a similar barrier length of 1.65 lattice constants reduces forward transmission by four orders of magnitude. This measurement further confirms that the backward modes are purely evanescent, and not merely lossy. If lossy backward-propagating modes existed in the

system, a large defect would have scattered a significant portion of energy into them, essentially converting backscattering into loss. The forward transmission in the presence of the large defect would have been much smaller than in the defect-free case. Existing optical isolators, such as those relying on Faraday rotation or nonreciprocal phase shifts, absorb or radiate backward-propagating light in this way. Thus, the unidirectional guiding of a CES is fundamentally different from how optical isolators operate.

The experimental establishment of topological photonic states opens up a wide range of exciting future opportunities. First, our realization of nontrivial topological Chern numbers in a classical photonic system raises the possibility of using photonic systems to realize other classes of topological quantum numbers that have invoked intense interest in condensed-matter physics. Examples include the Z_2 topological number associated with the quantum spin Hall effect[19-22] and the "Hopf number" in certain 3D insulators[23]. Photonic crystals are attractive for such investigations because one can assign parameters such as lattice constants and unit cell geometries in a fully controlled manner[16], in contrast to most electronic systems. Second, the fact that the CESs in the present system are robust against disorder ensures that the design is tolerant towards fabrication imperfections, such as variations in the lattice constant, or the exact position of the guiding edge; this could enable implementation of extraordinarily robust waveguides. Finally, photonic CESs might prove useful in applications involving isolators[24] or slow light[25,26]. In conventional slow-light systems, disorder induces backscattering that increases quadratically with reduced group velocity[27], making them very sensitive to disorder. Although the present experiments have been conducted at GHz frequencies, this operating frequency can be increased simply by applying a stronger DC magnetic field[18]. Extension into the THz range might be achieved through metamaterials that resonantly enhance the magnetic activity[28-30]. Further extension to the optical regime is challenging, given the losses and weak gyrotropic effects in currently-known materials.

Methods Summary

Construction of the magnetically gyrotropic PhC. The gyromagnetic PhC was implemented with a square array (lattice constant: 40 mm) of vanadium-doped calcium-iron-garnet (VCIG, TCI ceramics NG1850) rods. Balancing the need for a large Voigt parameter against the drawback of absorption loss in the vicinity of the ferromagnetic resonance (5.6GHz), we designed the rod radius to be 3.9 mm and the lattice constant a to be 40 mm in order to maximize the bandwidth of the band gap without suffering excessive loss. A 16x10 array was used to measure the band gap of a bulk crystal and a 16x7 array is used to study the waveguide and the effect of scattering. The VCIG ferrite features a measured permittivity ε_r=14.63 and a loss tangent tanδ=0.00010. The saturation magnetization was measured to be M_s=1.52x10^{5}A/m, with a 3dB linewidth of the ferromagnetic resonance at ΔH=1.03x10^{3}A/m. By using the MIT cyclotron electromagnet, we applied a DC magnetic field of 0.20T along the out-of-plane z-direction, with a spatial non-uniformity of less than 1.5%. The DC magnetic field breaks the time-reversal symmetry in the PhC. The magnetic field strength was measured and calibrated with a LakeShore 410 Gaussmeter.

Methods

Parallel plate waveguide for out-of-plane confinement. The unidirectional CES waveguide apparatus was designed to reproduce the dispersion relation and the modal profile of a topological edge mode of a 2D gyromagnetic PhC, using a 3D structure with a finite height. The out-of-plane z-confinement was achieved with two parallel horizontal copper plates, separated by 7.0mm. This structure is known as a "parallel plate waveguide" in microwave engineering[18]. It supports TEM modes with electric fields pointing in the out-of-plane z-direction and magnetic fields pointing along the x-y plane. This polarization is identical to the TM modes in 2D PhCs where topological modes have been proposed to exist[7]. Between the two plates, the electromagnetic fields of TEM modes are also uniform along the z-direction, identical to a 2D

system. This 3D structure therefore closely mimics a 2D system and is considered to be quasi-2D. When operated below 21GHz, the waveguide supports only TEM modes.

Single-mode microwave CES waveguide and absorbing boundaries. Similar to the case of conventional waveguides, if the edge waveguide has too large a cross-section area, this could lead to a multimode operation, causing both a unidirectional CES as well as conventional *bidirectional* modes to be present in the waveguide. To ensure that only a CES is present in the measurement setup, we chose the distance between the PhC and the conducting copper wall to be 25mm, narrow enough to eliminate all *bidirectional* modes at the frequencies of the second band gap. With a 6% relative bandwidth for this band gap, a CES is confined within three lattice constants, even around a large scatterer. The copper scatterer has a height of 7.0 mm and a width of 7.2mm, with its maximum length used in this experiment was mainly limited by the finite size of the crystal. Microwave-absorbing foam pieces were placed along the other three edges of the PhC, in order to prevent the CES from circulating all the way around the boundary of the crystal. In addition, these foam pieces shield the system from external interference.

Microwave transmission measurement for bulk crystals and for CESs. Two identically-constructed antennas were inserted through the top copper plate, extending to contact the bottom copper plate. These antennas, labelled A and B in Fig. 1a, were connected via coaxial cables to the two ports of a Hewlett-Packard 8719C vector network analyzer, which measures the transmission coefficients S_{AB} and S_{BA}. Two-port short-open-load-through (SOLT) calibrations were performed at the coaxial adapter. Therefore, measured S-parameters contain a frequency-dependent insertion loss from the impedance mismatch between the antenna, the feed coax, and the PhC waveguide, and from the transition between the balanced parallel plates and the unbalanced coax cable. This loss is reciprocal and does not affect the relative ratio of the transmission coefficients, $|S_{AB}/ S_{BA}|$. Therefore, any substantial difference between $|S_{AB}|$ and $|S_{BA}|$ is an experimental signature of the unidirectionality of CESs. We extracted the forward and backward transmission spectra from the measured S_{21} and S_{12} parameters in a frequency sweep

from 1GHz to 6GHz. Each measurement was performed with an IF frequency of 20Hz and 4 averages, with the power level normalized towards the level at the band edges. To measure bulk band gaps (Fig. 3a), the antennas A and B are located along the long axis of a 16 x 10 PhC, 8 lattice constants apart (see supplementary information). For the CES waveguide (Figs. 3c and 4), we performed the measurement with the feed and probe antennas located between the copper wall and the 16 x 7 PhC, also 8 lattice constants apart (Fig. 1a). Here the metal wall is 9mm away from each antenna.

Effects of material absorption loss. Most of the propagation loss in the present system may be attributed to two sources: the radiation losses originating from the finite width of the PhC cladding, and the intrinsic material absorption associated with the ferromagnetic resonance. The radiation loss could be further reduced simply by increasing the number of unit cells in the lateral direction, whereas the absorption loss could in principle be further reduced by using mono-crystalline Yttrium-Iron-Garnet as ferrites[18]. The resultant attenuation length would be on the order of hundreds of lattice constants.

1. von Klitzing, K., Dorda, G. & Pepper, M., New method for high-accuracy determination of the fine-structure constant based on quantized Hall resistance. *Phys. Rev. Lett.* **45**, 494 (1980).

2. Tsui, D. C., Stormer, H. L. & Gossard, A. C., Two-dimensional magnetotransport in the extreme quantum limit. *Phys. Rev. Lett.* **48**, 1559 (1982).

3. Novoselov, K. S. et al., Two-dimensional gas of massless Dirac fermions in graphene. *Nature* **438**, 197-200 (2005).

4. Zhang, Y. B., Tan, Y. W., Stormer, H. L. & Kim, P., Experimental observation of the quantum Hall effect and Berry's phase in graphene. *Nature* **438**, 201-204 (2005).

5. Haldane, F. D. M. & Raghu, S., Possible realization of directional optical waveguides in photonic crystals with broken time-reversal symmetry. *Phys. Rev. Lett.* **100**, 013904 (2008).

6. Raghu, S. & Haldane, F. D. M., Analogs of quantum-Hall-effect edge states in photonic crystals. *Phys. Rev. A* **78**, 033834 (2008).

7. Wang, Z., Chong, Y. D., Joannopoulos, J. D. & Soljacic, M., Reflection-free one-way edge modes in a gyromagnetic photonic crystal. *Phys. Rev. Lett.* **100**, 013905 (2008).

8. Prange, R. E. & Girvin, S. M. eds., *The Quantum Hall effect*. (Springer-Verlag, 1987).

9. Thouless, D. J., Kohmoto, M., Nightingale, M. P. & Dennijs, M., Quantized hall conductance in a two-dimensional periodic potential. *Phys. Rev. Lett.* **49**, 405-408 (1982).

10. Simon, B., Holonomy, the quantum adiabatic theorem, and Berry phase. *Phys. Rev. Lett.* **51**, 2167-2170 (1983).

11. Kohmoto, M., Topological invariant and the quantization of the Hall conductance. *Ann. Phys.* **160**, 343-354 (1985).

12. Haldane, F. D. M., Model for a quantum Hall effect without Landau levels: condensed-matter realization of the "parity anomaly". *Phys. Rev. Lett.* **61**, 2015 (1988).

13. Hatsugai, Y., Chern number and edge states in the integer quantum Hall effect. *Phys. Rev. Lett.* **71**, 3697 (1993).

14. Yablonovitch, E., Inhibited spontaneous emission in solid-state physics and electronics. *Phys. Rev. Lett.* **58**, 2059-2062 (1987).

15. John, S., Strong localization of photons in certain disordered dielectric superlattices. *Phys. Rev. Lett.* **58**, 2486-2489 (1987).

16. Joannopoulos, J. D., Johnson, S. G., Winn, J. N. & Meade, R. D., *Photonic Crystals: Molding the Flow of Light*. (Princeton University Press, 2008).

17. Chong, Y. D., Wen, X. G. & Soljacic, M., Effective theory of quadratic degeneracies. *Physical Review B* **77**, 235125 (2008).

18. Pozar, D. M., *Microwave* Engineering, 2nd ed. (John Wiley, 1998).

19. Murakami, S., Nagaosa, N. & Zhang, S.-C., Dissipationless Quantum Spin Current at Room Temperature. *Science* **301**, 1348-1351 (2003).

20. Kane, C. L. & Mele, E. J., Z(2) topological order and the quantum spin Hall effect. *Phys. Rev. Lett.* **95**, 146802 (2005).

21. Bernevig, B. A., Hughes, T. L. & Zhang, S. C., Quantum spin Hall effect and topological phase transition in HgTe quantum wells. *Science* **314**, 1757-1761 (2006).

22. Hsieh, D. et al., A topological Dirac insulator in a quantum spin Hall phase. *Nature* **452**, 970-975 (2008).

23. Moore, J. E., Ran, Y. & Wen, X.-G., Topological Surface States in Three-Dimensional Magnetic Insulators. *Phys. Rev. Lett.* **101**, 186805 (2008).

24. Yu, Z. F. & Fan, S. H., Complete optical isolation created by indirect interband photonic transitions. *Nature Photonics* **3**, 91-94 (2009).

25. Baba, T., Slow light in photonic crystals. *Nature Photonics* **2**, 465-473 (2008).

26. Thevenaz, L., Slow and fast light in optical fibres. *Nature Photonics* **2**, 474-481 (2008).

27. Povinelli, M. L. et al., Effect of a photonic band gap on scattering from waveguide disorder. *Appl. Phys. Lett.* **84**, 3639-3641 (2004).

28. Pendry, J. B., Holden, A. J., Robbins, D. J. & Stewart, W. J., Magnetism from conductors and enhanced nonlinear phenomena. *IEEE Trans. Microwave Theory Tech.* **47**, 2075-2084 (1999).

29. Yen, T. J. et al., Terahertz magnetic response from artificial materials. *Science* **303**, 1494-1496 (2004).

30. Linden, S. et al., Magnetic response of metamaterials at 100 terahertz. *Science* **306**, 1351-1353 (2004).

Supplementary Information accompanies the paper on **www.nature.com/nature**.

Acknowledgements We are very grateful to Peter Fisher and Ulrich J. Becker for generously providing access to the MIT synchrotron magnet. We should like to thank Isaac Chuang, Peter Bermel, Jorge Bravo-Abad, Steven Johnson, and Peter Rakich for many helpful comments. This work was supported in part by the MRSEC Program of the National Science Foundation under award number DMR-0819762, and also in part by the U.S Army Research Office through the Institute for Soldier Nanotechnologies under Contract No. W911NF-07-D-0004.

Author contributions Z.W., Y.C, J.D.J, and M.S. designed the photonic crystal system, analyzed the data and wrote the manuscript. Z.W., Y.C. fabricated the structure and performed all the experimental measurements.

Author Information Reprints and permissions information is available at npg.nature.com/reprintsandpermissions . Correspondence and requests for materials should be addressed to Z.W. (zhwang@mit.edu)

FIGURE LEGENDS

Figure 1 Microwave waveguide supporting CESs. a, Schematic of the waveguide composed of an interface between a gyromagnetic PhC slab (blue rods) and a metal wall (yellow). The structure is sandwiched between two parallel copper plates (yellow) for z-direction confinement and surrounded with microwave absorbing foams (gray regions). Two dipole antennas A and B serve as feeds and/or probes. A variable-length (*l*) metal obstacle (orange) with a full height of the waveguide (7.0 mm) is inserted between the antennas to study scattering. A 0.20T DC magnetic field is applied along the z-direction with an electromagnet (not shown). **b**, Top view (photograph) of the actual waveguide with the top plate removed.

Figure 2 Photonic CESs and effects of a large scatterer. a, CES field distribution (E_z) at 4.5 GHz in the absence of the scatterer, calculated from finite-element steady-state analysis (COMSOL Multiphysics). The feed antenna (cyan star), *omnidirectional* in homogeneous media (see supplementary information), radiates *only* to the right along the CES waveguide. Black arrows represent the direction of the power flow. **b**, When a large obstacle (3 lattice-constants long) is inserted, forward transmission remains unchanged since back- and side-scattering are entirely suppressed. The calculated field pattern illustrates how the CES wraps around the scatterer. **c**, When antenna B is used as feed antenna, negligible power is transmitted to the left, since the backward modes are evanescent.

Figure 3 CES-facilitated waveguiding in a PhC. a, Forward and backward transmission spectra measured using *only* the bulk PhC in the Fig. 1 setup (*i.e.* without the metal cladding and obstacle), with the antennas placed at the interior of the PhC, in a 0.20T DC magnetic field. The bulk transmission is reciprocal, with photonic band

gaps at 3.3 and 4.5 GHz. **b**, Calculated projected PhC band structure (blue and grey areas). Included is the CES (red curve) that exists at the metal/PhC interface. The grey areas are bulk bands with ill-defined band-edges due to large absorption near the ferromagnetic resonance. Each band's Chern number is labelled in white. **c**, Measured transmission spectra upon inclusion of the metal cladding and antennas placed as shown in Fig. 1. The resulting CES waveguide leads to a very high contrast between the forward and the backward transmission for frequencies in the second band gap (yellow) around 4.5GHz. This striking unidirectionality indicates the existence of a CES.

Figure 4 CES transmission spectra in the presence of a large scatterer. The length of the obstacle (l) was gradually varied from 0.40a to 1.65a (lattice constant a=40mm) and induced only minor differences in the forward transmission near the mid-gap frequency of 4.5 GHz. The lack of any significant changes in forward transmission and non-reciprocity ($|S_{AB}|<<|S_{BA}|$) with large increases in the size of the scatterer, indicate that the CES can travel around the obstacle without scattering or reflections, as predicted by simulations. The experimental parameters remained unchanged from the measurement in Fig. 3c.

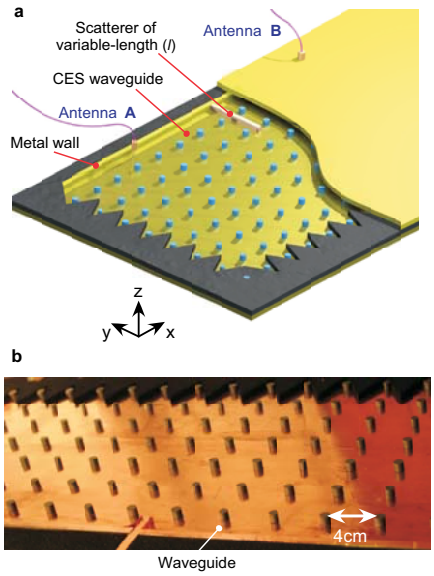
a
Scatterer of
variable-length (l)
Antenna B
CES waveguide
Antenna A
Metal wall
z
y
x
b
4cm
Waveguide

Figure 1

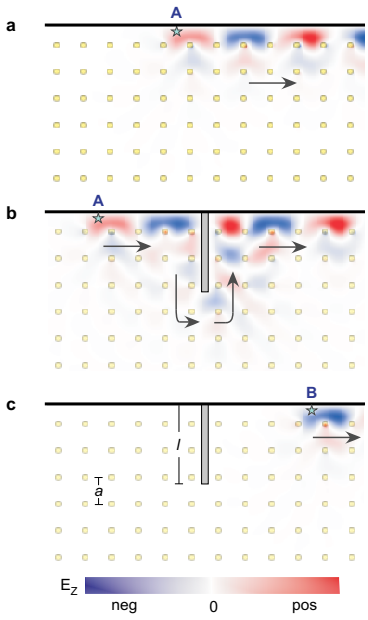

Figure 2

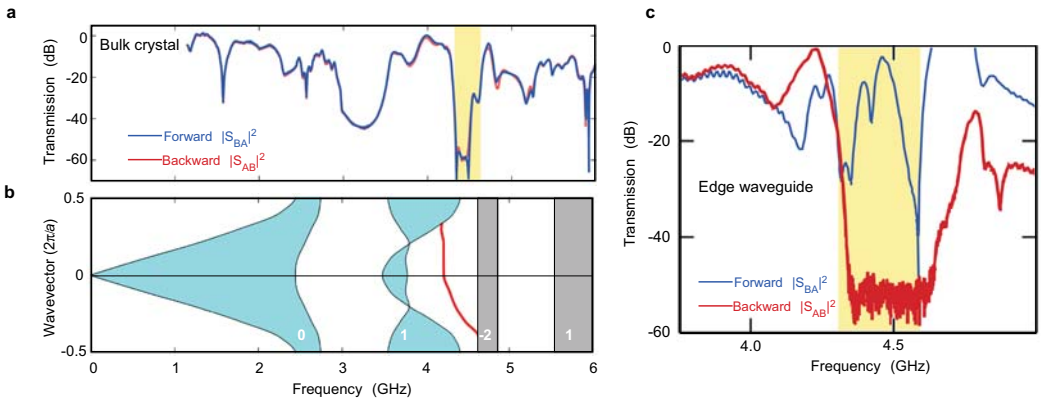
a
Bulk crystal
Transmission (dB)
0
-20
-40
-60
Forward $|S_{BA}|^2$
Backward $|S_{AB}|^2$
b
Wavevector ($2\pi/a$)
0.5
0
-0.5
0
1
-2
1
0
1
2
3
4
5
6
Frequency (GHz)
c
Edge waveguide
Transmission (dB)
0
-20
-40
-60
Forward $|S_{BA}|^2$
Backward $|S_{AB}|^2$
4.0
4.5
Frequency (GHz)

Figure 3

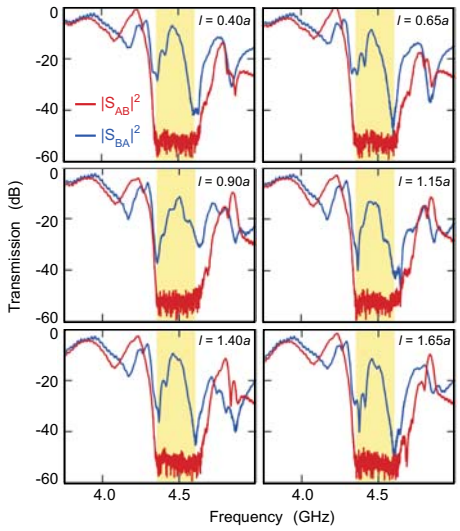
0
-20
-40
-60
l = 0.40a
|S_AB|^2
|S_BA|^2
l = 0.65a
l = 0.90a
l = 1.15a
l = 1.40a
l = 1.65a
Transmission (dB)
4.0
4.5
Frequency (GHz)

Figure 4